The 20th International Conference on
TRANSPORT AND SEDIMENTATION OF SOLID PARTICLES
26–29th September 2023, Wroclaw, Poland

ISSN 0867-7964 ISBN 978-83-7717-392-3

PARAMETER MATCHING OF DEEP-SEA POLYMETALLIC NODULE COLLECTION DEVICE BASED ON THE COANDĂ-EFFECT

Jianxin XIA[1,3*], Qiang YANG[1,3], Shen LIU[1,3], Guangzhi LIU [2]

DOI: 10.30825/4.14-20.2023

[1] *School of Ocean Sciences, China University of Geoscience, Beijing, 100083, China*
[2] *Beijing Institute of Exploration Engineering, Beijing, 100083*
[3] *Key Laboratory of Polar Geology and Marine Minerals of Ministry of Education, Beijing, 100083*
[*] *e-mail: jxxia@vip.sina.com*

ABSTRACT**:** Deep-sea mineral resources are becoming an essential guarantee for humankind's future socioeconomic sustainable development due to the decrease in terrestrial mineral resources. Collection devices, as vital components of deep-sea mining systems, need to address the efficiency of collection and the environmental disturbances caused by mining activities. The present study investigated the influence of the angle of jets and the radii of a convex wall on the flow field inside the Coandă-effect-based collection device to optimize the collection device using a numerical approach. The results indicated: (1) the increase of the angle of jets and radii of a convex wall of the collection device improved flow field uniformity, and the kinetic energy of flow concentrated in the bottom region. The higher mobile speed of the collection device induced a greater Coandă-effect beneath the convex wall. The internal flow field remained relatively stable when the device was at a speed of 0.5 m/s. (2) the angles of jets and the radii of the convex wall had a significant correlation with the lift and drag force on the nodule. The lift force on the nodule increased when a larger angle of jets or smaller radii of the convex wall occurred in the present study. (3) after analysing the transportation path of nodule particles in stages of separating, lifting, and carrying, it was found that the collection device accurately captured the nodules into the inlet in the scenarios that the collection device had a height of 80 mm above the seafloor and an input jet with an angle of 45°meanwhile the convex wall had a radius of 350 mm with the collection device movement at a speed of 0.5 m/s. This study provides important guidelines for the design and development of deep-sea polymetallic nodule collection devices.

KEYWORDS: polymetallic nodules; Coandă-effect; deep-sea mining; parameter matching; motion feature.

1. INTRODUCTION

Polymetallic nodules in the deep-sea sediment, which have a high mining value due to their wide distribution, high abundance, and large storage of important strategy metals such as Mn, Co, Ni, etc. are usually partially or fully buried and widely distributed in sea-bed at a depth of 4-6 km (Xin, 2013). As the International Seabed Authority addressed high concerns about the environmental impact of the mining process and the

profitability of the mining process, the deep-sea polymetallic mining equipment is preferable to the design with low disturbance to the deep-sea environment and high mining efficiency (Yang, 2000).

Seabed mining system works on the surface of seabed sediments, so this process directly affects the important indexes of the system such as collection efficiency and environment-friendly (Fan, 2021). The Coandă-effect-based collection device first appeared in the polymetallic nodule collection experiment conducted by Japan at a depth of 2,200 m in 1997, with a collection efficiency of about 87% (Yamada, 1998). Rodman et al. mathematically demonstrated that the collection of a Coandă-effect-based device was achieved by the low-pressure area near the wall caused by a tangential jet of a certain velocity to a curved wall (Rodman, 1989), thus, the pressure difference generated with the seafloor enhanced the collection of polymetallic nodules. Yue et al. simulated numerically the mining process to contrast the three hydraulic mining methods, including a mining head based on the Coandă effect in order to optimize the collection method (Yue, 2021). The study found that the Coandă effect-based suction collection device had low-energy consumption and minimal environmental disturbance when the three collection methods, with a collection efficiency (η) of 80%. Kim et al. established a computational model to predict the Coandă effect-based device collection efficiency using a reliability-based design optimization method (RBDO) (Kim, 2019). The computational model adjusted the design parameters of the collection device with the physical parameters of the manganese nodules. As for the research on optimizing the collection efficiency of the collection device, Lee et al. found that the height of the collection device over the seafloor, the radius of the convex wall, the velocity of jet flow, and the nozzle shape .were affecting the collection efficiency (Lee, 2013). According to the DY-69 voyage report, the size of the manganese nodules was 50-100 mm. Jia Hao's numerical results indicated that the lift force on the particles significantly decreased when the particle size was too large (Jia, 2022). The aforementioned scholars have conducted impressive research on the optimal design of the collection device. However, they lack an overall consideration of flow field data and did not conduct force analysis on the motion state of the nodules.

This study worked on the optimal designs of the Coandă-effect-based collection device for the deep-sea polymetallic nodule using numerical modelling methods. Various angles of jets and radii of the convex wall of the collection device model were established using the Design Modeler module in Ansys software. We numerically obtained the flow field off the collection device in motion states and analysed the effects of the motion speed of the collection mechanism and the angle of jets on the flow field. As such, we completed the optimization of the collection device by analysing the three stages of Separating, lifting and carrying of nodule motion by utilizing the occurrence status and physical character of the nodules in the Western Pacific.

2. NUMERICAL METHODS AND MODEL DESIGN

2.1. NUMERICAL METHODS

Ansys software was used to conduct a numerical simulation of the collection device. Incompressible fluid continuity equation and the momentum equation in the Navier-Stokes equations are (Dai, 2018):

$$\frac{\partial \rho_l}{\partial t}+\frac{\partial \rho_l u_i}{\partial x_i}=0 \tag{1}$$

$$\frac{\partial \rho_l u_i}{\partial t}+\frac{\partial \rho_l u_i u_j}{\partial x_j}=-\frac{\partial P}{\partial x_i}+\frac{\partial}{\partial x_i}\left[\left(\mu+\mu_t\right)\left(\frac{\partial u_i}{\partial x_j}+\frac{\partial u_j}{\partial x_i}\right)\right] \tag{2}$$

where ρ_l is the fluid density, t is time, x_i and x_j are the horizontal and vertical coordinates, u_i and u_j are the velocity components of the fluid in the horizontal and vertical directions, P is pressure, μ is molecular viscosity, and μ_t is turbulent kinetic viscosity.

In the Realizable K-Epsilon model, the dissipation rate equation is derived through an exact transport equation for the turbulent kinetic energy fluctuation. Compared to the K-Epsilon model, the Realizable K-Epsilon model used a superior turbulence model in addressing complex boundary flow problems. The model can be expressed as follows (Shaheed, 2019):

$$\frac{\partial k}{\partial t}+\frac{\partial k u_i}{\partial x_i}=\frac{\partial}{\partial x_i}\left(Dk_{\text{eff}}\frac{\partial k}{\partial x_i}\right)+G_k-\varepsilon \tag{3}$$

$$\frac{\partial \varepsilon}{\partial t}+\frac{\partial \varepsilon u_i}{\partial x_i}=\frac{\partial}{\partial x_i}\left(D\varepsilon_{\text{eff}}\frac{\partial \varepsilon}{\partial x_i}\right)+\sqrt{2}C_{1\varepsilon}S_{ij}\varepsilon-C_{2\varepsilon}\frac{\varepsilon^2}{k+\sqrt{\mu\varepsilon}} \tag{4}$$

where k is turbulent kinetic energy, ε is turbulent dissipation rate, the effective diffusivity coefficient for k is denoted as Dk_{eff}, and the turbulent viscosity coefficient for ε is denoted as $D\varepsilon_{\text{eff}}$. G_k is turbulent kinetic energy under the influence of velocity mean gradient, S_{ij} is the strain rate tensor, with a value of 1.3, $C_{1\varepsilon}$=1.44, and $C_{2\varepsilon}$=1.92.

2.2 MODEL DESIGN

In the Design Modeler module, the collection device model is created, as shown in Fig.1. Existing studies have shown that when the nodule size is too large, the lifting force on the nodule becomes less (Jia, 2022). Dual-jets injection elevated the ore by eroding the sediment at the bottom of the ore deposit (Guan, 2021). The single-row nozzle jets design of Global Sea Mineral

Resources (GSR) in Belgium was modified by adding a deflector at the jets outlet to allow part of the inlet jets to directly erode the bottom sediment through the deflector.

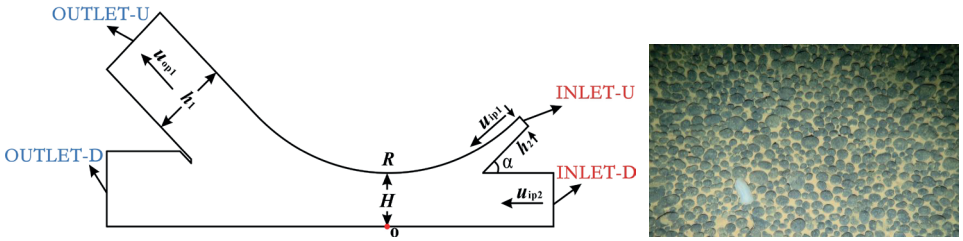

Fig. 1 Collection device model settings and nodule occurrence phases

The flow field variations under four angles of jets and three radii convex walls were applied in Tab. 1 based on existing research findings and the current lab scenarios (Guan, 2021; Hu, 2022; Yue, 2021).

Table 1

Parameter of angles of jets and radii of the convex wall of the collection device

α/ (°)	30			35			40			45		
R/(mm)	250	300	350	250	300	350	250	300	350	250	300	350

The height of inlet was set to 120 mm, and the height of jets outlet was set to 20 mm. Ten rectangular jets nozzles were centrally arranged, with each nozzle having a width of 40 mm and a spacing of 10 mm. The height H of the concave wall above the bottom was related to the pressure gradient height of flow, which directly affected the lift index of manganese nodules (Jia, 2022). Therefore, the height H required to match the occurrence state of nodules on the seabed (Fig. 1). In this study, the height H above the bottom was set to 80 mm. If all nodules are in a fully buried state in a certain mining area, the height of collection device above the seafloor required to be adjusted appropriately to increase collection efficiency (Peng, 2020) (Tab. 2).

Table 2

Collection device parameter settings

Parameter	Value	Definition
u_{op1} /(m/s)	3	velocity of outlet
u_{ip1} /(m/s)	10	velocity of inlet
u_0 /(m/s)	0.5	velocity of collection device
H /mm	80	height of convex wall above the bottom
h_1 /mm	120	height of outlet
h_2 /mm	20	height of inlet

This study considered two working scenarios (Fig. 2) including scenario I, OUTLET+INLET and scenario II, OUTLET+INLET+MOVING. Then, three observation lines were set up. L1 line was set as the perpendicular line from the lowest point of the convex wall to the bottom surface. OT1 Line was set at the beginning of the inlet. OT2 Line was set at the beginning of the lower inlet. An O-xyz Cartesian coordinate system was used in the 3D space, where the origin O was set at the intersection point of the perpendicular line from the center of the lowest point of the convex wall to the lower plane.

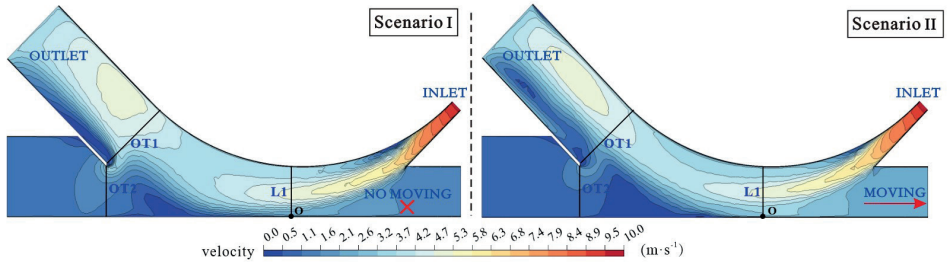

Fig. 2 Two numerical simulation scenarios

It is assumed in the numerical simulation that the nodules' influence on the flow field is negligible due to the complexity of the problem. The study (Wang, 2000) indicated that the upper 50 mm of the deep-sea was mainly compromised of loose and soft sediments in a semi-liquefied state. The jets action of the collecting device eroded the loose sediment around the nodules during collecting (Oebius, 2001). As such, only water layers were applied.

The computational grid was generated using the Fluent-Meshing tool, and a hexahedral grid was used to partition the computational domain. The independence of mesh was analyzed. The structural parameters R = 350 mm and $\alpha = 45°$ are used for validation without motion velocity. The time step Δt was set to 0.00010 s, and the minimum grid size Δl was varied (0.0050 m, 0.0010 m, 0.0005 m, and 0.0001 m) to calculate the velocity at the midpoint of OT2 under four different cases while keeping other variables constant. The results of mesh convergence were shown in Fig. 3(a). A grid size of Δl = 0.0005 m was applied to ensure mesh independence and reduce computational effort. Further, the velocity at the midpoint of OT2 was used to compare with four-time steps (Δt = 0.00100 s, 0.00050 s, 0.00010 s, and 0.00005 s) to verify the time step independence of the numerical method as shown in Fig. 3(b). A time step of Δt = 0.00010 s was used for numerical calculations, as the four different time steps showed good agreement.

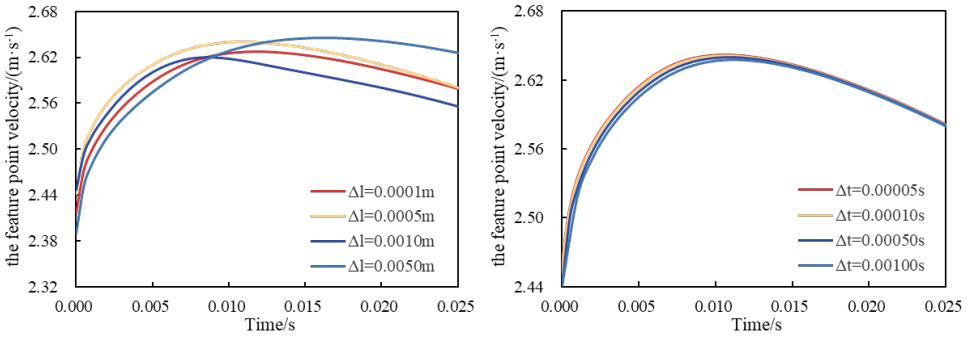

(a) Mesh convergence test (b) time step convergence test

Fig. 3 Grid and time step verification

3 NUMERICAL ANALYSIS AND RESULTS

3.1 NUMERICAL SIMULATION RESULTS FOR SCENARIO I

The flow field displayed significant wall attachment phenomena in scenario I as shown in Fig. 4. As the height above the bottom increased at L1, the flow velocity gradually increased. A sharp decrease of flow velocity was observed near convex wall. At OT1, the overall velocity was smaller than at L1. An increase in the height above the bottom was occurred at OT2. The flow velocity had an exponential increase, and the high-energy region of the flow field was mainly concentrated in the top region.

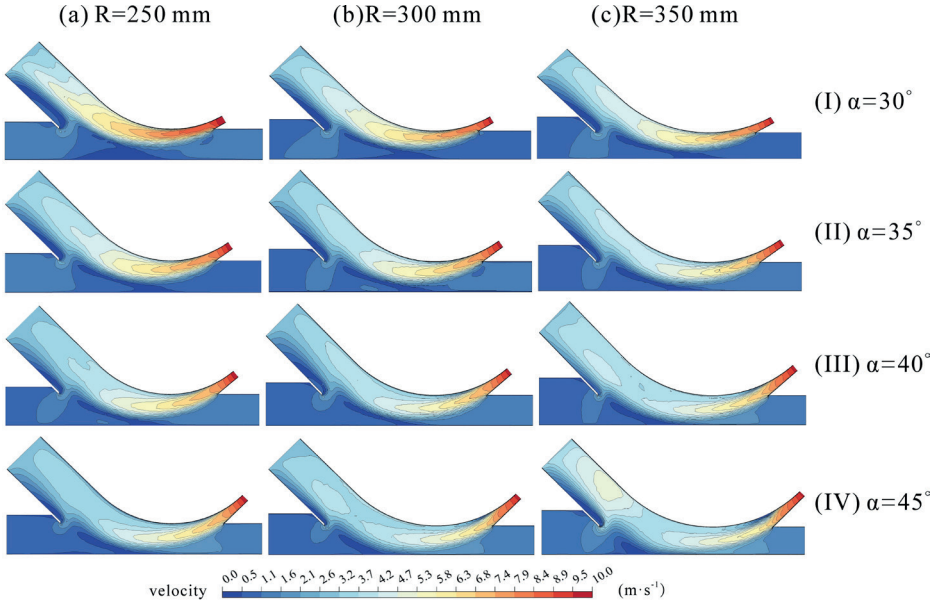

Fig. 4 Flow velocity cloud diagram under working scenario I

3.2 NUMERICAL SIMULATION RESULTS FOR SCENARIO II

By comparing scenario, I and II (Fig. 4 and Fig. 5) and taking the case of R=350 mm and α=45° as an example, it was observed that the mean flow velocity at L1 increased from approximately 3.50 m/s to 4.11 m/s. $\bar{u}$ at OT2 decreased from2.51 m/s to 1.91 m/s. An increase of the motion velocity of the collection device led to a significant decrease of σ which indicated that the higher motion velocity enhanced the Coandă-effect below convex wall favoring the stability of the internal flow field. However, it weakened the kinetic energy of the flow within the OT2 plane, resulting in less capacity of the flow to capture the nodules at OT2.

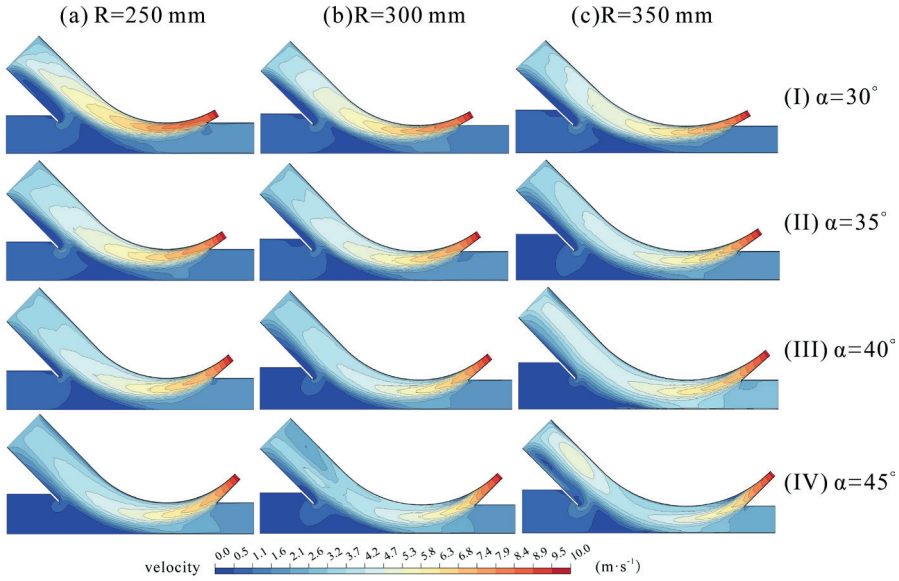

Fig. 5 Flow velocity cloud diagram under working scenario II

4 ANALYSIS OF MOTION FEATURES AND PARAMETER MATCHING

Based on previous study and the analysis of the flow field, this study characterized the motion of nodule into three stages: Separating, lifting, and carrying. Based on this division, the parameters of the collecting device were matched as follows. By optimizing the collecting device, the pressure gradient force generated by the jets was increased enhancing the removal of the nodules. In the lifting stage, both the jets and suction effects contributed to the lifting process of the nodules, on which were acted both upward lift force due to the pressure gradient and drag force exerted by the flow field. In the carrying stage, the main action was suction, which rapidly transported the nodules into the inlet (Fig. 6).

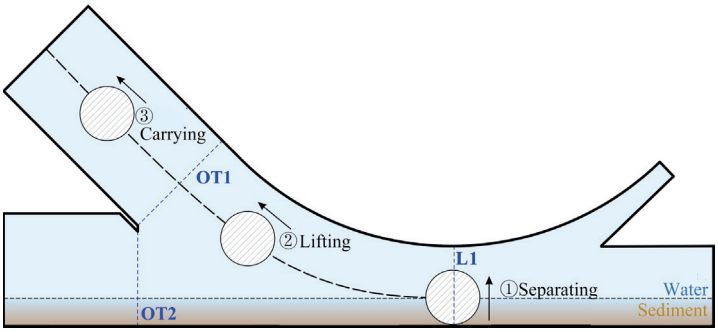

Fig. 6 Particle movement stage division during the mining process

4.1 FACTORS AFFECTING THE MOTION OF NODULES WITHIN THE COLLECTING DEVICE.

Based on the Coandă effect, the collecting device utilized wall-bounded jets to create pressure differences around the nodules. When a pressure gradient existed, it exerted a force on the particles, resulting in lifting the nodules. In addition to gravity, other factors that were affecting the motion of nodules within the collecting device include pressure gradient in the vertical direction, which was calculated using the following formula:

$$F_{\mathrm{P}} = -V_{\mathrm{n}} \frac{\partial p}{\partial y} \tag{5}$$

where V_{n} was the volume of nodules, $\partial p / \partial y$ was the pressure gradient, and F_{P} was the pressure gradient force.

It was assumed that the nodules were uniform spherical bodies with a diameter D in the present study. The pressure difference $\mathrm{d}P$ acted on a set of horizontally symmetrical annular elements on the surface of the nodules. Then, the pressure gradient dF_{P} was given by:

$$F_{\mathrm{P}} = -\frac{D^2}{2}\pi \int_0^{\frac{\pi}{2}} \left[P(y_1) - P(y_2)\right] \sin\delta \cos\delta d\delta \tag{6}$$

In the equation:

$$y_1 = y_{\mathrm{o}} + \frac{D}{2}\cos\delta \tag{7}$$

$$y_2 = y_o - \frac{D}{2}\cos\delta \tag{8}$$

where δ was the angle between the normal pressure and the vertical direction at a certain point on the nodule's surface, y_o was the height of the center of mass of the nodules above the bottom, y_1 and y_2 are the heights of a set of horizontally symmetrical annular elements relative to the center of mass of the nodules.

The drag force exerted by the fluid on the particles considering the pressure gradient force while neglecting particle self-rotation was calculated by:

$$F_D = \frac{\pi}{8} C_D D^2 \rho_l \left|u_l - u_n\right| \left(u_l - u_n\right) \tag{9}$$

where u_l was the fluid velocity, u_n was the motion velocity, C_D was the drag coefficient.

The empirical formula for the drag coefficient of particles at high Reynolds numbers (Re=10,000−50,000) was obtained from experiments(Morsi, 1972):

$$C_D = \frac{-1662.5}{Re} + \frac{5.4167\times10^6}{Re^2} + 0.5191 \tag{10}$$

After equations (10) them into equation (9), resulting in:

$$F_D = \frac{\pi}{8} D\left(-1662.5\mu\left(u_l - u_n\right) + \frac{5.4167\times10^6\mu^2}{\rho_l D} + 0.5191\rho_l D\left|u_l - u_n\right|\left(u_l - u_n\right)\right) \tag{11}$$

In the equation, μ=1.01×10³ Pa·s, and u_l was greater than u_n; according to the survey results of the DY69-M2B1-PS01-BC02 station in the western Pacific during the 69th ocean expedition, the average size of nodules mostly had median diameter of D=60 mm with a wet density ρ_n of 1.91×10³ kg/m³. After substituting the selected nodule parameters for the mining area, Fig. 7 was obtained.

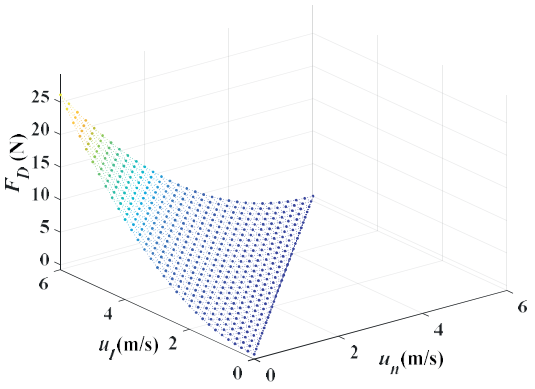

Fig. 7 The drag force F_D of nodules is related to u_t and u_n

4.2 PARAMETERS MATCHING FOR THE VARIOUS MOTION STAGES OF NODULES

4.2.1 SEPARATING STAGE

To simplify the discussion, the pressures labeled in Fig. 10 were relative values based on the pressure at the wall of the collection device with parameters R=250 mm and α=30° as the reference., it was observed that as the jets move along the curved wall as shown in Fig. 8. An uneven pressure field was observed at L1, with a low-pressure region near the convex wall. The pressure increased gradually with the decrease of H, and the pressure tended to be stable in the lower part of the section. Fig. 8(a) showed that as R increased, the pressure at the wall increased from 0 to about 2,000 Pa. This was due to the decrease of jets kinetic energy, which led to an increase in pressure for other scenarios. However, no significant difference in pressure was occurred near the ground. Fig. 8(b) indicated that an increase of angle of jets resulted in a decrease in pressure near the bottom, but the pressure gradient significantly increased. This may lead to an increase in the pressure gradient force acting on the nodules.

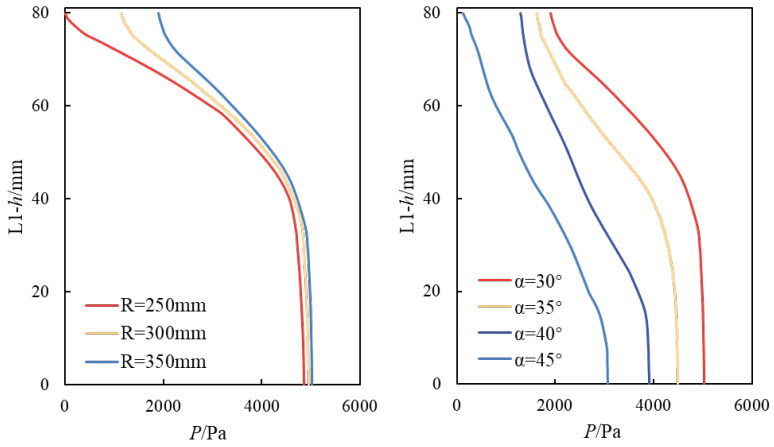

(a) Different curvature radii(α=30°) (b)Different jet anles(R=350 mm)

Fig. 8 Distribution of pressure field at the L1 line of different parameters

Based on the pressure field distribution, a third the order least squares fitting was performed on the pressure field distribution data at the L1 line of the collection device for various parameters at the initial position:

$$P(y) = p_1 \cdot y^3 + p_2 \cdot y^2 + p_3 \cdot y + C \tag{12}$$

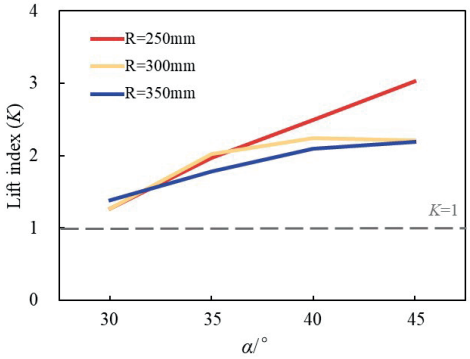

Fig. 9 Lift index at the L1 line

By substituting the obtained third-order polynomial fitting relationship into Equation (6) and solving the simultaneous equations (6) and (8), the pressure gradient force on the nodule at the critical state can be obtained. Neglecting the effects of fluid drag and viscosity, the lift index was defined as $K = F_p / G$. The

variation of the lifted force at the L1 section of the collection device for different parameter combinations was shown in Fig. 9. It was observed that the selected parameter combinations all resulted in a lift index greater than 1, indicating that the structural design optimization conducted in this study is beneficial for enhancing the lift index of large-sized nodules. Additionally, for the case of R=250 mm, the lift force showed a linear growth with the angle of jets. For the case of R=300/350 mm and α<40°, the angle of jets and lift force were roughly linearly correlated. However, when α≥40°, the increase of angle of jets had a less significant impact on the lift force.

4.2.2 LIFTING STAGE

Let u_{in} and u_{jn} be the velocity components of the nodule in the O-X and O-Y directions, respectively. The coordinates of the intersection points of OT1 and OT2 with the line were denoted as X and Y in the O-X and O-Y directions, respectively. The velocity increments of the nodule inside the flow field for each parameterized collection device were calculated in the O-X and O-Y directions based on the flow field results.

$$\begin{cases} \dfrac{\partial u_{\text{in}}}{\partial t} = \dfrac{6F_{\text{D}}\cos\delta}{\rho_{\text{n}}\pi D^3} \\ \dfrac{\partial u_{\text{jn}}}{\partial t} = \dfrac{6\left(F_{\text{D}}\sin\delta + F_P - G\right)}{\rho_{\text{n}}\pi D^3} \end{cases} \tag{13}$$

Based on the changes in pressure and velocity fields for each working scenario, by simultaneously solving equations (6) to (13) and iteratively calculating, the total motion times (t_i and t_j)required for the nodule to rise from point O to the target coordinates in the O-X and O-Y directions were obtained, as shown in Fig. 10. During the migration process, if the nodule's O-X coordinate was equal to the intersection coordinate, the motion time t_i was output. Subsequently, if the nodule's O-Y coordinate was equal to the intersection coordinate, then the motion time t_j was output. The iteration ended at this point, and this indicated that the nodule had actually reached the upper wall of the down suction pipe. Otherwise, if the nodule's O-Y coordinate was equal to the intersection coordinate first, it means that the nodule had entered the suction pipe.

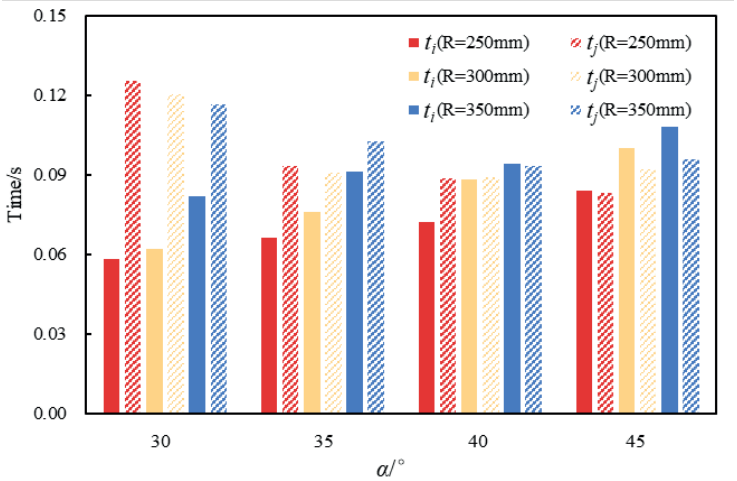

Fig. 10 Nodule movement time (and) in the O-X and O-Y directions

During the nodule lifting stage, the previous numerical simulations revealed [Oebius at al., 2001] that, the nodule may not completely enter OT1 but rather be dragged into OT2 by the flow field in the Coandă-effect-based collecting device, finally relying on the inlet flow for recollection. It was necessary to satisfy $t_i > t_j$ meaning that the nodule after lifting 80 mm can fully enter the suction inlet so that the nodule mostly entered OT1. As shown in Fig. 10, it can be observed that the angle of jets affects the lifting time of the nodule during the conveying stage, and the two are roughly positively correlated. When $\alpha < 40°$, for different radii of convex wall collecting devices, $t_i < t_j$ indicating that the nodule enters OT2. When $\alpha \geq 40°$, except for R=250 mm and α=40°, the nodule in the collecting device with different radii of convex wall satisfies $t_i > t_j$. Particularly, the matching relationship of the nodule of motion time was relatively well when the case had R of 350 mm and α of 45°.

4.3 CARRYING STAGE

The flow velocity of the collection device was required to exceed the free settling velocity of the nodule in the conveying stage while maintaining internal flow field uniformity to prevent nodule retention or sedimentation. The minimum flow velocity was required to prevent nodule sedimentation for a spherical nodule at the inlet in the turbulent zone was calculated using the particle settling velocity(Wu, 2000). The calculation method was as follows:

$$u_s = \frac{1.72\sqrt{gD(\rho_n - \rho_l)/\rho_l}}{\cos\delta} \tag{14}$$

Based on the design angle of the inlet, the minimum flow velocity required to maintain the upward movement of the nodule along the pipeline during the conveying stage was obtained by setting δ=45° in equation (14), and it was found to be 1.78m/s.

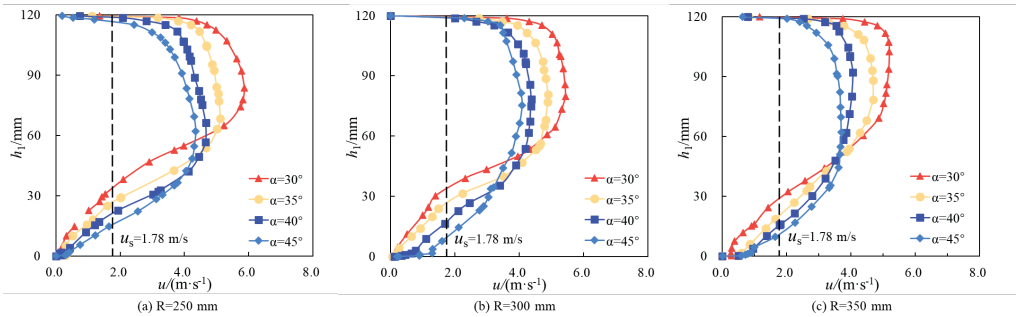

Fig. 11 Flow velocity distribution of OT1 line

An increase in the angle of jets was observed in Fig. 11. The velocity distribution below the OT1 section tended to become more uniform, and the range of velocities, that was less than u_s, gradually decreased. On the other hand, an increase of the radii of convex wall occurred, the range of velocities, which was smaller than u_s, decreased slightly. As discussed in Section 3, the velocity distribution was more uniform without significant changes. The flow field distribution was the most uniform in the cases of R=300/350 mm and α=45°, and the control of the relatively low-velocity region below the section was better, allowing the manganese nodule to maintain an upward conveying state regardless of its position during the conveying stage.

5. CONCLUSION

Computational Fluid Dynamics (CFD) method was conducted to investigate the parameter matching of a deep-sea polymetallic nodule of the Coandă-effect-based collection device. This study explored the influences the collection device at different motion scenarios, including angle of jets and radius of convex wall, on the internal flow field. The following conclusions were drawn from the present study:

(1) The angle of jets, radius of convex wall, and motion speed of the collection device significantly affect the flow field. The increase in the angle of jets resulted in more flow kinetic energy centered at the bottom region of the collection device, and this enhances the uniformity of the flow field at OT1. A larger radius of convex wall contributes to stabilize the uniformity of the flow field according to the various observation sections in the collection device, and a stronger constraint on the flow field at OT2 was observed. The motion speed of the collection device enhances the Coandă-effect below the convex wall,

leading to an increase of pressure gradient force on the nodules. When a collection device motions at a speed of 0.5 m/s, its internal flow field is relatively stable.

(2) The parameters of the collection device have a significant correlation with the lift and drag force on the nodule. The lifting force on the nodule increases as the angle of jets or radii of the convex wall of the collection device decreases. The parameter matching of the collection device controls the nodule motion state: the angle of the jets was linear-positively correlated with the lift force at R=250 mm in the separating stage. Additionally, influences of the collection device parameter on the lift force is not significant when R=300/350 mm and $\alpha > 40°$. A good matching relationship between nodule motion time and R=350 mm and $\alpha=45°$ is observed in the lifting stage. The flow field distribution is most uniform in the carrying stage when R=300/350 mm and $\alpha=45°$, and the control of the relatively low-velocity region at the bottom of the line is better ensuring, that the manganese nodules can be well transported upwards during this phase.

(3) Flow field inside the collection device was compared with the nodule's transportation path, and the matching correlation was proposed for some parameters of the collection device. When the collection device is at a height of 80 mm above the seafloor, the angle of jets α is 45°, the radii of convex wall R is 350 mm, and the motion speed is 0.5 m/s, the manganese nodules can more accurately enter the suction inlet. These research results provide important technical support for the design and development of deep-sea polymetallic nodule collection devices.

ACKNOWLEDGEMENTS

Financial support was received from the National Natural Science Foundation of China (U1906234 and 51339008), the National Key Research and Development Program of China (2021YFC2801500), and is gratefully acknowledged.

REFERENCES

1. Dai, B. and Chen, Z. M. 2018. Numerical simulation of flow field downstream of a submerged sluice gate based on the Realizable k-epsilon Model. *Journal of Water Resources and Architectural Engineering* 16(04), pp. 176-180.
2. Fan, Z. H. and Jia, Y. G. 2021. Review on potential engineering geological environment impacts of deep-sea polymetallic nodules mining. *Journal of Engineering Geology* 29(6), pp. 1676-1691.
3. Guan, L. and Zhang, D. K. 2021. Comparison and analysis of deep-sea polymetallic nodules collection methods and structural parameters. *Journal of Ocean Technology* 40(05), pp. 62-70.
4. Hu, J. C., Zhao, G. C., Xiao, L. 2022. F. Experimental investigation on flow field and collecting characteristics of mining device based on Coandă effect. *The Ocean Engineering* 40(05), pp. 132-138.

5. Jia, H., Yang, J., Su, X. Theoretical Prediction on Hydraulic Lift of a Coanda Effect-Based Mining Collector for Manganese Nodule. *Energies* 15(17), pp. 6345.
6. Kim, S., Cho, S. G., Lee, M. S. 2019. Reliability-based design optimization of a pick-up device of a manganese nodule pilot mining robot using the Coanda effect. *Journal of Mechanical Science and Technology* 33(08), pp. 3665-3672.
7. Lee, M., Hong, S., Choi, J. S. 2013. Design optimization of a hydraulic deep-sea manganese pick-up device using Coanda effect. [In:] *Proceedings of the KSME Fall Annual Meeting.* Busan: Korea, pp. 1660-1665.
8. Morsi, S. A., Alexander, A. J. 1972. An investigation of particle trajectories in two-phase flow systems. *Journal of Fluid Mechanics* 55(02), pp. 193-208
9. Oebius, H. U., Becker, H., Rolinski, S. 2001. Parametrization and evaluation of marine environmental impacts produced by deep-sea manganese nodule mining *Deep Sea Research Part II: Topical Studies in Oceanography* 48(17), pp. 3453-3467
10. Peng, J. P. 2020. Research on controlling ground clearance of hydraulic collectors in polymetallic nodules mining. *Mining and Metallurgical Engineering* 40(03), pp. 20-23
11. Rodman, L. C., Wood, N. J., Roberts, L. 1989. Experimental investigation of straight and curved annular wall jets. *AIAAJ* 27, pp. 1059-1067.
12. Shaheed, R., Mohammadian, A., Gildeh, H. K. 2019. A comparison of standard k–ε and realizable k–ε turbulence models in curved and confluent channels. *Environ Fluid Mech* 19, pp. 543-568.
13. Wang, S.R., Yang, N., Wang, G.M. 2000 Strength characteristics of deep sea deposits in China′s mining region in the pacific ocean′s C-C Zone. *Mining and Metallurgical Engineering* 20(03), pp. 21-24.
14. Wu, N., Zhang, Q., Qu, Z. Q. 2000. Evaluation on calculation methods of solid particle settling velocity in fluid. Oil Drilling & Production Technology 22(02), pp. 51-53.
15. Xin, R. Liu, H., Guan, X. Y. 2013. *Marine resources*. Beijing: Chemical Industry Press, 99 pp.
16. Yamada, H., Yamazaki, T. 1998. Japan's Ocean Test of the Nodule Mining System. [In:] *Proc 8th int Offshore Polar Eng Conf.* Montreal: Canada, pp. 13-19.
17. Yang, N and Xia, J. X. 2000. Development techniques for international sea-floor resources and their future trend. *Mining and Metallurgical Engineering* 20(01), pp. 1-4.
18. Yue, Z. Y., Zhao, G. C., Xiao, L. F.,. 2021. Comparative study on collection performance of three nodule collection methods in seawater and sediment-seawater mixture. *Applied Ocean Research* 110, pp. 102606.